J. Fluid Mech. (2009), vol. 636, pp. 137–153. © Cambridge University Press 2009
doi:10.1017/S0022112009007733

Symmetric Holmboe instabilities in a laboratory exchange flow

EDMUND W. TEDFORD[1]†, R. PIETERS[1,2]
AND G. A. LAWRENCE[1]

[1]Department of Civil Engineering, University of British Columbia, Vancouver, BC V6T 1Z4, Canada

[2]Department of Earth and Ocean Sciences, University of British Columbia, Vancouver, BC V6T 1Z4, Canada

(Received 8 September 2008; revised 16 April 2009; accepted 17 April 2009)

Laboratory experiments have been conducted that test the predictions of Holmboe (*Geofys. Publ.*, vol. 24, 1962, pp. 67–112). Symmetric Holmboe instabilities are observed during steady, maximal two-layer exchange flow in a long laboratory channel of rectangular cross-section. Internal hydraulic controls at each end of the channel isolate the subcritical region within the channel from disturbances in the reservoirs. Inside the channel, the instabilities form cusp-like waves that propagate in both directions. The phase speed of the instabilities is consistent with Holmboe's theory and increases along the length of the channel as a result of the gradual acceleration of each layer. This acceleration causes the wavelength of any given instability to increase in the flow direction until it is approximately twice the most amplified wavelength. At this point new waves develop with the result that the average wavelength is almost constant along the length of the channel.

1. Introduction

Flows in the environment often consist of well-defined layers of different densities. A density difference can result from salinity (e.g. in an estuary or the ocean), temperature (e.g. in a lake), sediment (e.g. gravity current) or other factors. Studies of geophysical flows have shown that wave-like features occur at the interface between sheared layers (Geyer & Smith 1987; Wesson & Gregg 1994; Tedford *et al.* 2009). As these interfacial features or instabilities grow, fluid is exchanged vertically between the layers. Mixing between layers is important because it controls the vertical transfer of salt, heat, nutrients, pollutants and momentum.

Stratified shear flows in the laboratory also exhibit a variety of wave-like features. The most well-known are the Kelvin–Helmholtz (KH) instabilities observed in the classic experiments of Thorpe (1971). In these experiments the shear between two homogeneous layers of slightly different salinity causes instabilities that are exceptionally uniform in wavelength and amplitude. These instabilities quickly grow into stationary billows which, in turn, break down into three-dimensional turbulence. Of the shear instabilities that occur in stratified flows, the KH instability has been studied most extensively, but in recent years increasing attention has been paid to the Holmboe instability.

---

† Email address for correspondence: ttedford@eos.ubc.ca

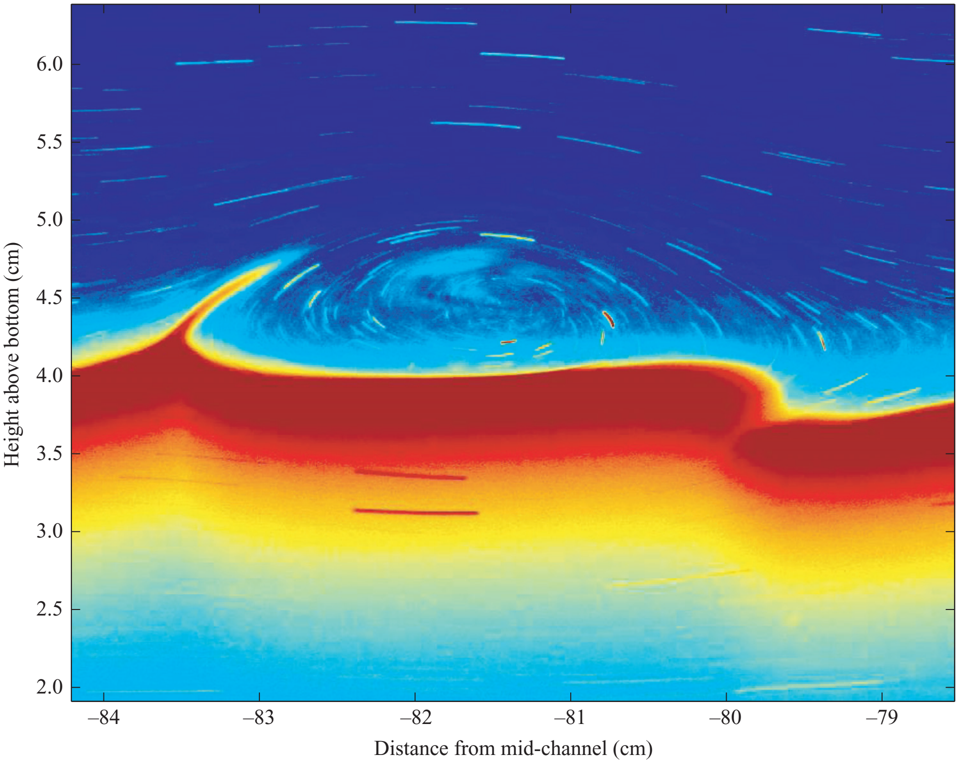

FIGURE 1. Close-up image of the interface between two layers. The upper fresh layer is moving to the right, and lower saline layer is moving to the left. The upward-pointing cusp is a positive, rightward-propagating Holmboe instability, and the downward-pointing cusp is a negative, leftward-propagating Holmboe instability. The colour varies from blue to red, marking high to low fluorescence of the dye. The decrease in fluorescence below the interface is caused by the dissipation of light. To generate particle streaks the shutter speed of the camera was set to 0.5 s.

Holmboe (1962) analysed the stability of a sharp density interface subjected to shear. He predicted that when stratification is strong enough to suppress the KH instability, two wavetrains develop that travel with equal and opposite phase speeds with respect to the mean flow. An example of Holmboe's instability from the present experiments is shown in figure 1. The potential importance of Holmboe instabilities was recently highlighted by the direct numerical simulations of Smyth & Winters (2003), who found that although Holmboe instabilities grow less rapidly than KH instabilities, the total amount of mixing can be greater (see also Smyth 2006; Carpenter, Lawrence & Smyth 2007; Smyth, Carpenter & Lawrence 2007). Note that while Holmboe (1962) assumed a density step, Alexakis (2005) has shown that Holmboe instabilities can occur, if the thickness of the velocity interface is more than double the thickness of the density interface. Holmboe instabilities are thought to occur in natural flows such as the exchange flow through the Strait of Gibraltar (Farmer & Armi 1998) and salinity intrusions in strongly stratified estuaries (Yoshida *et al.* 1998; Tedford *et al.* 2009).

Several techniques have been used to study Holmboe instabilities in the laboratory. In the splitter-plate experiments of Koop & Browand (1979) and Lawrence, Browand & Redekopp (1991) only one of the two modes predicted by Holmboe appeared.

A series of cusps from which wisps of interfacial fluid were occasionally ejected formed on only one side of the interface. This 'one-sidedness' was a result of a vertical displacement between the sharp density interface and the shear, an inherent condition in splitter-plate experiments. While Carpenter *et al.* (2007) have postulated that one-sided instabilities may be an important source of mixing, we will restrict our attention to symmetric (two-sided) instabilities in the present study.

Using immiscible fluids and varying viscosity, Pouliquen, Chomaz & Huerre (1994) conducted tilting-tube experiments to generate Holmboe instabilities. Due to the slow growth of the instabilities and the inherently short duration of tilting-tube experiments they were only able to observe the early onset of instabilities, and unlike Thorpe (1971), they were required to use regularly spaced obstacles to force uniformity.

The one-sidedness of splitter-plate experiments, and the short duration of tilting-tube experiments, can be avoided by using exchange flow. Zhu & Lawrence (2001) studied Holmboe instabilities in exchange flow through a channel of uniform width with a sill. However, symmetric Holmboe instabilities were only a transient feature of these experiments. Hogg & Ivey (2003) studied exchange flow through a contraction. However, this contraction was relatively short so that only a small number of instabilities were present at any given time, and the background flow conditions changed over a single wavelength. While the observations of Zhu & Lawrence (2001) provided some confirmation of the linear predictions of Holmboe (1962), Hogg & Ivey (2003) observed phase speeds that were significantly different from the linear predictions. In the present study we carefully examine the linear predictions using observations from a long channel of uniform cross-section in which many waves are present at any given time.

The goals of this study are to carry out experiments in the laboratory that generate Holmboe instabilities and to compare the properties of these instabilities with the predictions of Holmboe (1962). In the next section, the linear model of Holmboe (1962) is described. Section 3 describes the laboratory set-up and methods. In § 4, the evolution of the mean flow and the observed wave characteristics are described. In § 5, the observations are compared with the linear predictions.

2. Background theory

2.1. *Hydraulics of exchange flow*

The basic features of exchange flow can be described by two-layer hydraulics (Armi 1986). Here we briefly review the concept of internal hydraulic controls and their relevance to the instabilities. In single-layer flows the concept of 'hydraulic control' is used to determine how flow rate relates to channel geometry. A single-layer control can occur where the flow exits a restriction, such as a horizontal expansion or an increase in bed slope. At the control the flow speed is equal to the long-wave speed and is therefore said to be critical. In subcritical flow, waves may propagate in both directions, upstream and downstream. In supercritical flow waves can only propagate in one direction, downstream. At the control there is a transition from subcritical to supercritical flow.

Two-layer flows also exhibit hydraulic controls, but their occurrence is complicated by factors such as flow in both directions, channel geometry influencing each layer differently, shear influencing the long-wave speed and mixing between the layers. Although waves can form on both the free surface and the interface between the layers, here we are solely concerned with interfacial (internal) waves and instabilities.

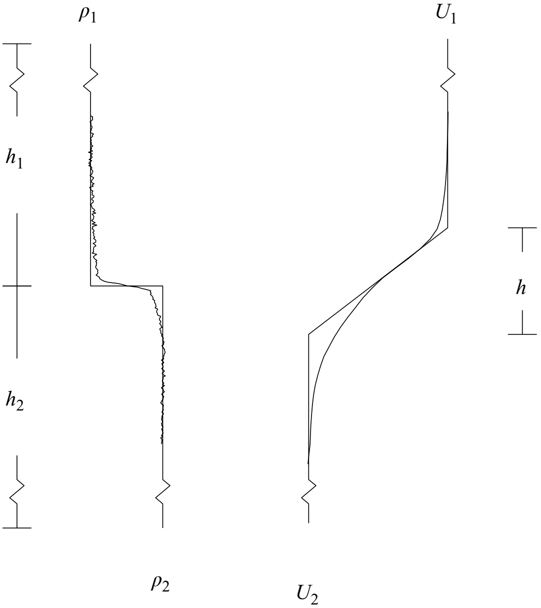

FIGURE 2. Definition sketch for piecewise linear profiles used in the analysis of Holmboe instabilities. Also shown are sample density and velocity profiles from the current study.

Similar to single-layer flows an internal control occurs at a transition from subcritical to supercritical flow. In subcritical flow, internal waves, including instabilities, may propagate in both directions. In supercritical flow they can propagate in only one direction. In the present study we focus on maximal exchange flows, which are characterized by a control at each end of the channel (Gu & Lawrence 2005). The flow is subcritical within the channel and supercritical outside of it. In the supercritical regions just outside of the channel, waves can only propagate away from the channel; i.e. waves from the reservoirs cannot enter the channel.

2.2. *Dispersion relation and instability*

To investigate the dynamics of instabilities, Holmboe (1962) analysed the piecewise linear velocity and density profiles shown in figure 2. The sharp density interface within a uniform shear layer approximates conditions observed in salt-stratified shear flows at laboratory scales; sample profiles from the present experiments are shown in figure 2. Holmboe's analysis assumes the density interface is centred within the shear layer and does not account for the influence of the boundaries. The key parameters in the stability analysis are the velocity difference between the layers $\Delta U = U_1 - U_2$, the shear-layer thickness $h = \Delta U/(\mathrm{d}U/\mathrm{d}z)_{max}$ and the reduced gravitational acceleration, $g' = g\Delta\rho/\rho_0$ (where $\Delta\rho$ is the density difference and ρ_0 is the average density). The subscripts 1 and 2 indicate the upper and lower layers, respectively. To characterize the total shear across the interface, U_1 and U_2 are defined as the free-stream velocity in each layer.

The shear and stratification parameters are combined to form the bulk Richardson number $J = g'h/\Delta U^2$. Following Holmboe's analysis, Lawrence *et al.* (1991) used the Taylor–Goldstein equation to relate the complex phase speed ($c = c_r + \mathrm{i}c_i$) to the

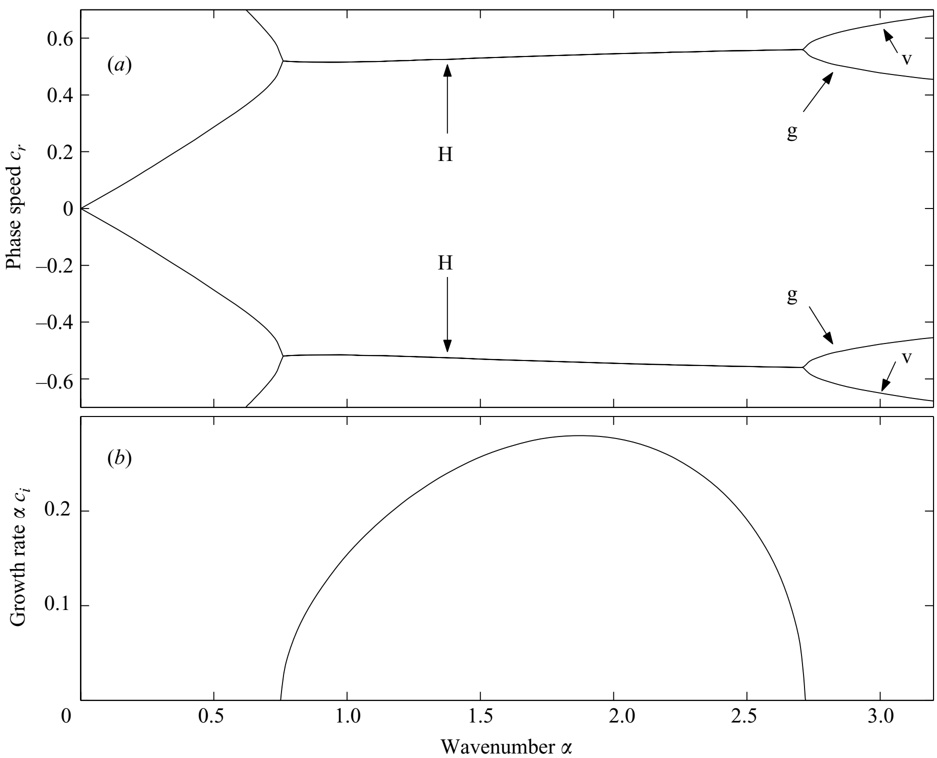

FIGURE 3. (*a*) Dispersion relation for the Holmboe flow configuration at $J = 0.3$. The labels H, v and g indicate line segments associated with Holmboe (unstable), vorticity and gravity modes respectively. (*b*) Exponential growth rate (αc_i) of the Holmboe mode. The wavenumber of maximum growth ($\alpha = 1.9$) corresponds to a dimensional wavelength $\lambda \approx 7\,\mathrm{cm}$ for the present experiments. The phase speed is shown non-dimensionalized by $\Delta U/2$; the wavenumber is non-dimensionalized by the shear-layer thickness h; and the growth rate is non-dimensionalized by $2h/\Delta U$.

wavenumber (α) and J:

$$c^2 = \frac{-a_1 \pm \sqrt{{a_1}^2 - 4a_2}}{2}, \tag{2.1}$$

where

$$a_1 = \beta_+\beta_- - n^2, \quad a_2 = n^2\beta_-^2, \quad \beta_\pm = [e^{-\alpha} \pm (1-\alpha)]/\alpha, \quad n^2 = 2J/\alpha.$$

For brevity, all of the terms in (2.1) are non-dimensional, and the phase speed is relative to the mean of the free-stream velocities, $\bar{U} = (U_1 + U_2)/2$. The dimensional phase speed is $c^* = c\ \Delta U/2 + \bar{U}$, and the dimensional wavelength is $\lambda = 2\pi h/\alpha$.

The dispersion relation (2.1) is plotted in figure 3 for $J = 0.3$ corresponding to conditions in our laboratory experiments (table 1). At high wavenumber the flow supports two stable gravity modes and two stable vorticity modes (so called because wave propagation is governed by buoyancy in the first instance and by the vorticity gradient in the second). The rightward-propagating vorticity mode is associated with the upper vorticity interface (upper kink in the velocity profile), and the leftward-propagating vorticity mode is associated with the lower vorticity interface. As the wavenumber decreases the vorticity mode and gravity mode propagating in the same direction merge into one unstable mode ($\alpha \approx 2.7$). At lower wavenumber ($\alpha \lesssim 0.75$)

H (cm)	L (cm)	W (cm)	g' (cm s^{-2})	h (cm)	ΔU (cm s^{-1})	J
10.8	200	10	1.39	2.1	3.1	0.3

TABLE 1. Experimental parameters.

the dispersion relation bifurcates back to four stable modes. Unlike the KH instability, the unstable mode particular to the Holmboe configuration is non-stationary.

When $J = 0.3$ the maximum growth rate of the Holmboe instability, $\alpha c_i = 0.28$, occurs at $\alpha = 1.9$ (figure 3*b*) with a corresponding phase speed $c_r = \pm 0.53$. Dimensionalization by $h = 2.1$ cm and $\Delta U/2 = 1.56$ cm s^{-1}, as observed in our experiments, yields a maximum growth rate at a wavenumber $k = 2\pi/\lambda = 0.9$ cm^{-1} ($\lambda = 7$ cm) and a phase speed of $c_r^* = \bar{U} \pm 0.83$ cm s^{-1}. The dimensional growth rate $kc_i^* = 0.2$ s^{-1} results in a doubling time of 3.5 s. In the following sections we will compare the observed wave characteristics with predictions from (2.1), particularly at the wavenumber of maximum growth.

3. Experimental set-up

A schematic of the laboratory set-up is shown in figure 4. The overall tank was 370 cm long, 106 cm wide and 30 cm deep as in Zhu & Lawrence (2001). The tank was divided into two equally sized reservoirs and connected by a channel 10 cm wide and 200 cm long. The water was well mixed between the reservoirs to ensure uniform temperature (≈ 20°C) throughout the tank. A removable gate was placed in the middle of the channel isolating the left and right sides. Salt was mixed into the right reservoir to provide a density difference of 1.41 kg m^{-3} (g' of 1.39 cm s^{-2}). The basic experimental parameters are provided in table 1.

The experiments differ from those of Zhu & Lawrence (2001) in that the water depth was kept relatively shallow ($H = 10.8$ cm), and there was no sill in the channel (flat bottom). These changes resulted in more gradual horizontal variations in U and J and therefore more uniform wave properties. In addition, the shallower depth resulted in a prolonged period of maximal exchange. Experiments using yet shallower depths or smaller density differences were attempted but resulted in the suppression of instabilities (presumably due to viscous effects). Larger density differences were also used but were subject to a number of problems including shortened experiment duration, large changes in the index of refraction at the density interface and diminished image quality (due to the higher shutter speeds required to capture faster waves). To gather the data used in this study the experiment was repeated 16 times with depth and $\Delta\rho$ held constant (see table 2).

Laser-induced fluorescence (LIF) was used to visualize the density interface by illuminating fluorescein dye in the lower layer with a continuous 4 W argon-ion laser. The laser beam was passed through a Powell lens to generate a downward-radiating light sheet along the centre of the channel. Images were collected using a digital camera; a sample image is shown in figure 4(*b*). The interface was identified by locating the maximum vertical gradient in light intensity.

A Dantec particle image velocimetry (PIV) system was used to measure the velocity of pliolite VT-L particles (Goodyear Chemical Co.). The particles were pulverized and sieved to obtain those with diameters less than 0.24 mm. While these particles are slightly denser than water ($\rho \approx 1030$ kg m^{-3}) their settling time is much longer than

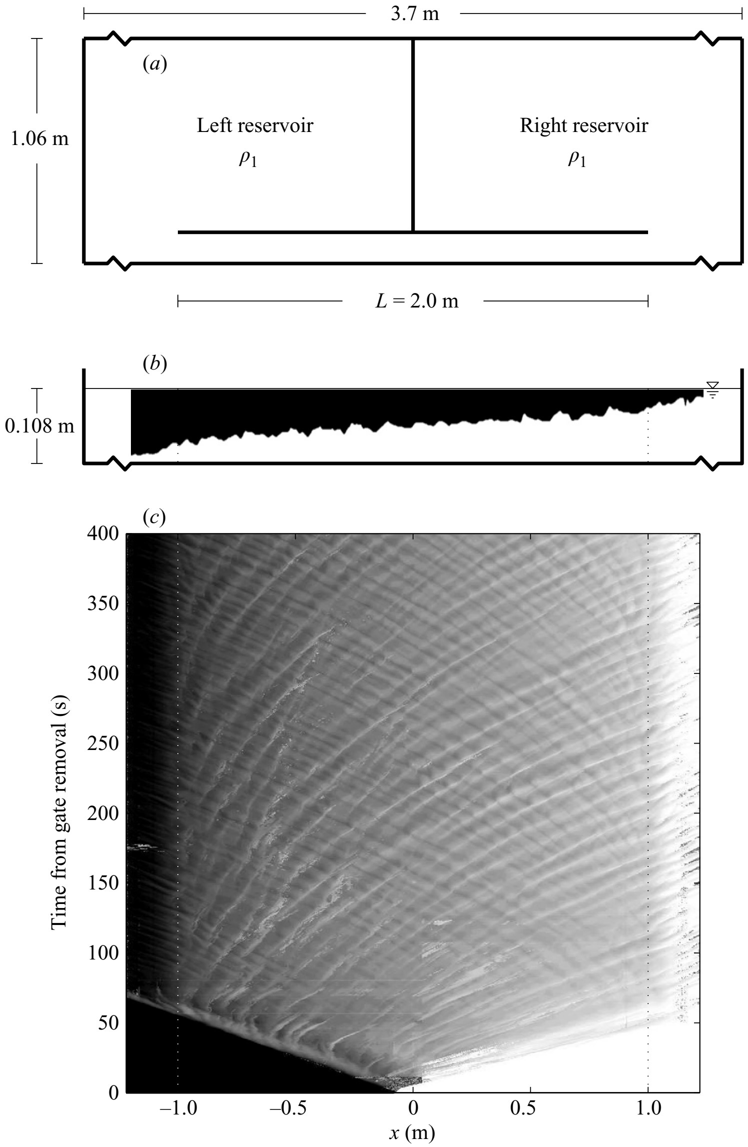

FIGURE 4. (*a*) Plan and (*b*) side view of the experimental set-up and (*c*) plot of wave characteristics. The left and right reservoirs initially contain fresh and saline water respectively. The side view (*b*) includes a sample image of the interface over the entire length of the channel plus a portion of each reservoir at $t = 400$ s. The lower layer contains dye and is illuminated from above with a laser-generated light sheet. The characteristics (*c*) represent a compilation of interface heights observed in several thousand images. The shading is scaled such that black indicates the interface is near the bottom of the channel, and white indicates the interface is near the free surface. Diagonal light and dark streaks represent interfacial waves.

the duration of the experiment. Pairs of images ($\Delta t = 0.04$ s) were collected every 3 s. A three-step adaptive correlation algorithm was used to calculate velocities. The final interrogation areas were 32 pixels wide and 16 pixels high (2.8 mm × 1.4 mm) with a 50 % overlap resulting in a 0.7 mm vertical spacing of vectors. The total image size was 11 cm wide and 9 cm high. Small scratches on the acrylic wall limited PIV to

Experiment	Measurement	Location	Replicates	Parameter	Figure
1–7	LIF	$-0.9 < x < 0.9$	7	h_2	6, 8, 9
8–12	PIV	$x = 0$	5	h, U_1, U_2	5, 6
13	LIF	$-1.2 < x < 1.2$	1	h_2	4, 7
14	PIV and LIF	$x = 0$	1	h, U_1, U_2	2
15	Particle streak	$x = -0.8$	1	–	1
16	Bottle samples	$x = -1, 0, 1$	1	g'	–

TABLE 2. Summary of laboratory experiments.

a single location ($x = 0$). The Dantec system was also used to determine density by quantitative measurement of dye fluorescence.

In experiment 13, LIF was performed over the entire viewable region of the tank ($-1.2\,\mathrm{m} < x < 1.2\,\mathrm{m}$). This experiment allowed us to include the critical and supercritical regions of the flow in our qualitative description of the wave characteristics. In experiment 14 both PIV and LIF were performed simultaneously to confirm that the density interface was much thinner than the shear layer (figure 2). Particle streak images (figure 1) were collected in experiment 15 to examine the structure of individual instabilities. Finally, fluid samples were collected with a syringe and analysed in a densitometer to verify $\Delta\rho$ between the layers.

4. Evolution of mean flow

The experiment begins when the gate separating the fresh and the salt water at the centre of the channel is removed. Two gravity currents immediately form and propagate in opposite directions; these gravity currents exit the channel at $t \approx 60\,\mathrm{s}$ (figure 4*c*). The gravity currents generate mixed fluid which is gradually flushed out of the channel, leaving two uniform layers separated by an interface approximately 2 mm thick ($t \approx 200$ s). In addition a barotropic oscillation known as Helmholtz resonance (Miles & Munk 1961) is generated when the gate is removed. This oscillation has a period of 28 s and persists until $t \approx 400\,\mathrm{s}$ (figure 5).

Once the Helmholtz oscillations dampen out, the flow enters a long period of relatively steady maximal exchange, which ends when the control at the right end of the channel is flooded, and the flow becomes subcritical in the right reservoir. After the control is lost, disturbances can enter the channel from the reservoir (not visible in figure 5). In the present study we focus on instabilities generated within the channel during the long period of maximal exchange when conditions are steady ($400\,\mathrm{s} < t < 800\,\mathrm{s}$). During this period interfacial wave properties remain relatively constant.

For the steady period the mean interface height shows a gradual slope (≈ 0.02) throughout most of the channel (figure 6*a*); a steeper slope occurs at the ends of the channel, consistent with the presence of controls. The observed interface height compares well with the analytical predictions of Gu & Lawrence (2005) with their $\alpha = 0.41$ and $r = 1$. The time-averaged velocity profile observed at $x = 0$ is shown in figure 6(*a*). At this point the average flow speed in each layer is $1.1\,\mathrm{cm\,s^{-1}}$. This is just over half the flow speed predicted by the inviscid two-layer theory ($\sqrt{g'H}/2 = 1.9\,\mathrm{cm\,s^{-1}}$).

The observed velocity profile can be approximated by a piecewise linear fit with free-stream (maximum) velocities in the upper and lower layers of $U_{1c} = 1.55\,\mathrm{cm\,s^{-1}}$

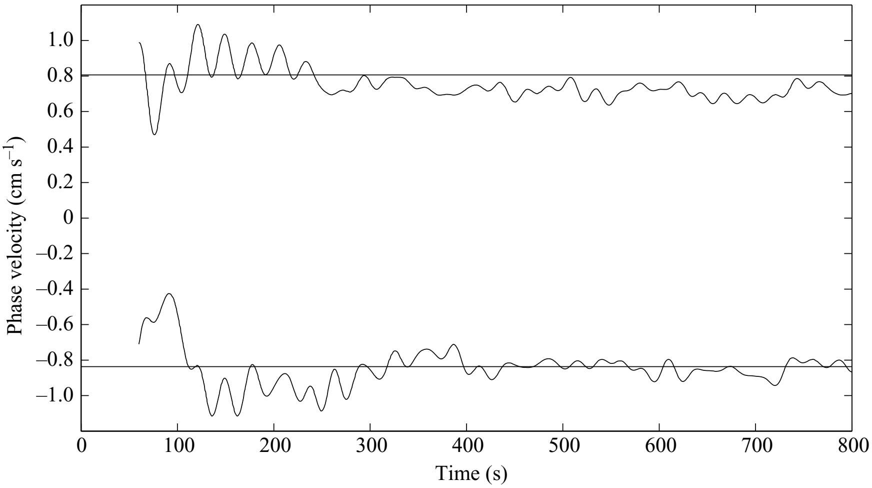

FIGURE 5. Phase velocities of rightward-propagating (positive) and leftward-propagating (negative) waves at $x = 0$. The phase velocities were calculated using the cross-correlation of the interface between successive images. Oscillations with periods less than 20 s have been filtered out. Helmholtz resonance with a period of 28 s is evident for $t < 400$ s. The horizontal lines are the phase speeds predicted using the linear theory.

and $U_{2c} = -1.57\,\mathrm{cm\,s^{-1}}$, respectively. The subscript c denotes the centre of the channel ($x = 0$). Because of the bottom boundary layer the lower layer has a slightly greater maximum velocity than the upper layer, resulting in $\bar{U}_c \approx -0.01\,\mathrm{cm\,s^{-1}}$. The velocity profile has a shear-layer thickness $h = 2.1$ cm.

To understand the evolution of the waves discussed in the next section it is useful to estimate the mean $\bar{U}(x) = (U_1(x) + U_2(x))/2$ along the entire length of the channel. We assume that $U_1(x)$ and $U_2(x)$ can be estimated from the velocities observed at the centre of the channel using $U_i(x) = U_{ic}y_{ic}/y_i(x)$, where the layer thicknesses y_i are based on the observed interface height (figure 6*a*). The resulting velocity estimates are plotted in figure 6(*b*) and will be used below to describe the evolution of the waves.

5. Wave evolution

The two waves in figure 1 exhibit the classic features of fully developed Holmboe instabilities. The upward-pointing (positive) cusp is moving to the right with the upper layer, and the downward-pointing (negative) cusp is moving to the left with the lower layer. The positive cusp is ejecting a wisp of interfacial fluid into the upper layer. The particle streaks indicate an elliptical vortex leading the positive cusp. The centre of the vortex has nearly stationary particles and is well above the density interface. Such vortices are typically present in numerical simulations of these flows (e.g. Smyth & Winters 2003) and play an important role in the generation of the wisps. The vortex carries partially mixed interfacial fluid back towards the cusp in which there is a horizontal convergence. The convergence at the cusp carries the fluid vertically away from the interface. These wisps of mixed fluid either can get caught in the leading vortex or, in some cases, are ejected above the vortex into a region of decreased shear and higher velocity. A similar vortex leads the lower cusp. Its presence is masked by the dye in the lower layer.

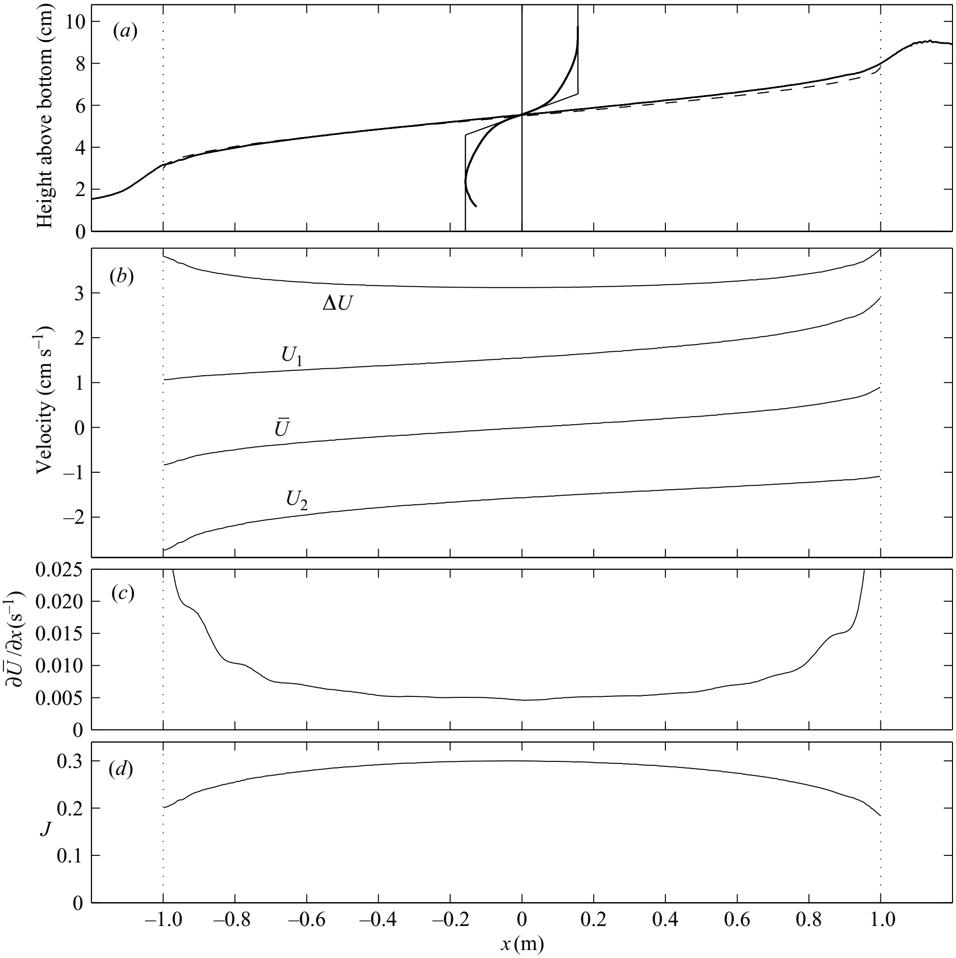

FIGURE 6. (*a*) Mean interface height along the channel during the period of steady exchange. The interface height predicted by two-layer hydraulics (see the text) is shown as a dashed line. Also shown is the average velocity profile observed at $x = 0$ and the piecewise linear profile used in the stability analysis. The maximum speeds in the upper and lower layers at $x = 0$ are $U_1 = 1.55\,\mathrm{cm\,s^{-1}}$ and $U_2 = -1.57\,\mathrm{cm\,s^{-1}}$ respectively. (*b*) Estimates of the free-stream (maximum) velocities $U_1(x)$ and $U_2(x)$, the total shear $\Delta U(x)$ and the mean velocity $\bar{U}(x)$. (*c*) Horizontal gradient in the mean velocity $\partial\bar{U}(x)/\partial x$. (*d*) Bulk Richardson number. The vertical dotted lines show the locations of the channel ends.

During the steady period (400–800 s) there is a roughly even distribution of rightward- and leftward-propagating waves as can be seen in the diagram of the characteristics given in figure 7(*b*). The characteristics represent a compilation of the interface height observed in a sequence of several thousand images (e.g. the image in figure 4*b*). The time-averaged interface height (figure 6*a*) has been removed, and the shading is scaled such that black indicates the trough of an instability, and white indicates the crest. White and black diagonal lines represent the propagating cusps of positive and negative instabilities, respectively. In general the instabilities form quickly (<20 s) and maintain a nearly constant amplitude while they are within the channel. Despite irregularities in the characteristics the instabilities can be filtered

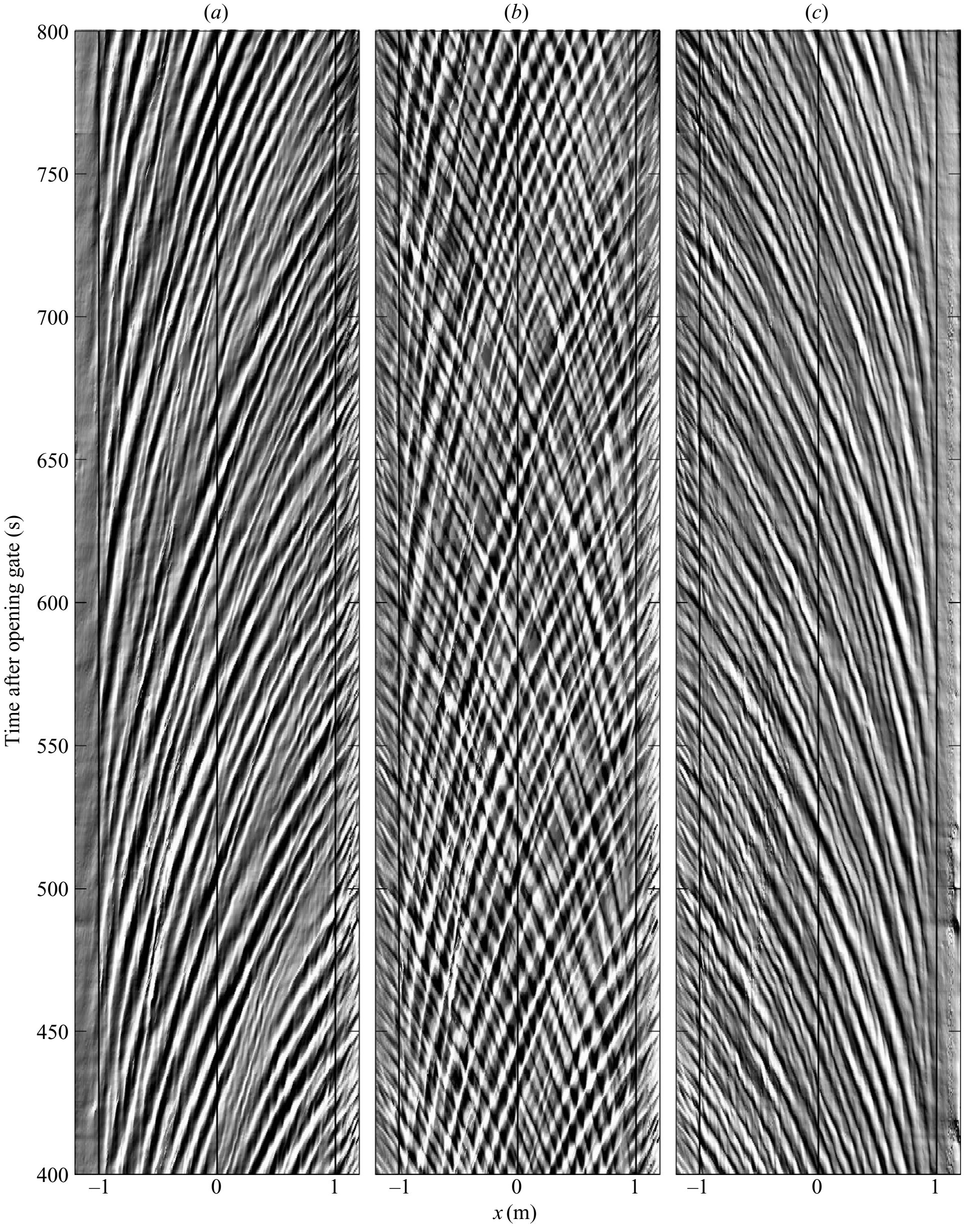

FIGURE 7. Characteristics during the period of steady exchange. The shading indicates the deviation of the interface elevation from the mean. Pure white (black) indicates a positive (negative) deviation greater than 3 mm. The characteristics in (*b*) were split into (*a*) rightward- and (*c*) leftward-propagating components using the two-dimensional FFT. The ends of the channel are at $x = \pm 1$ m.

into distinct rightward- and leftward-propagating (figures 7*a* and 7*c* respectively) components using the two-dimensional fast Fourier transform (FFT).

The influence of the controls can be seen in the characteristics at the ends of the channel ($x = \pm 1$ m; figures 7*a* and 7*c*). Within the channel, disturbances move in both directions (subcritical), and beyond the ends of the channel they only move outward into the reservoirs (supercritical). Although difficult to see, both upward- and downward-cusping modes are propagating outward in the supercritical regions (e.g. figure 7*c*; $x = -1.05\,\mathrm{m}$, $t = 625$–$650\,\mathrm{s}$). As expected the controls block disturbances from entering the channel; i.e. waves propagating within the channel have formed there rather than within the reservoirs. Because one of the two Holmboe modes is stationary near each control, the separation of the modes using the two-dimensional FFT is less effective near the ends of the channel. In addition, the nearly stationary waves near the ends of the channel have a very low frequency resulting in very few waves per experiment and therefore greater uncertainty in quantifying wave properties. For these reasons our analysis below will focus on $-0.9\,\mathrm{m} < x < 0.9\,\mathrm{m}$.

To further illustrate the wave evolution we have traced out the crests of a set of the positive, rightward-propagating waves (figure 8*a*). At the left end of the channel four wave crests pass $x = -0.9$ m over a period of approximately 110 s, indicating a wave period of 37 s (frequency $\omega = 0.027\,\mathrm{Hz}$). At $x = +0.9\,\mathrm{m}$, there is still 110 s between the first and last wave crests; however, here there are 13 wave crests in total, indicating an average wave period of 9.2 s ($\omega = 0.11\,\mathrm{Hz}$). This increase in frequency is a result of new waves forming throughout the channel.

The frequency evolution is quantified by counting all of the zero crossings that occur over the period of steady exchange (400 s) and averaging over seven experiments (experiments 1–7). The characteristics were low-pass filtered (wavelengths $> 1\,\mathrm{cm}$) before counting the zero crossings to minimize the upward bias associated with noise. As in the traces, the zero crossings show an increase in the number of positive waves from left to right (figure 8*b*). The negative waves show the same accumulation in the opposite direction.

The formation of new waves is related to the changes in phase velocity that the waves undergo as they propagate along the channel. The phase velocity of a wave is given by the inverse of the slope of its characteristic ($\mathrm{d}x/\mathrm{d}t$). A nearly vertical line indicates a slow-moving wave, while a nearly horizontal line indicates a fast-moving wave. The positive (rightward-propagating) waves shown in figure 8(*a*) therefore accelerate from left to right (the traced lines become more horizontal). The dominant phase velocity of the waves (i.e. the slope of the wave characteristics) is determined by cross-correlating time series of the interface height at adjacent locations along the channel. This phase velocity is calculated for experiments 1–7 and then averaged (figure 8*c*). The average shows that both the positive and negative waves accelerate as they propagate along the channel.

The wave acceleration is most easily understood by considering the variation in the mean velocity $\bar{U}$ over the length of the channel (figure 6*b*). The mean velocity is replotted in figure 8(*c*) and shows a slope that is similar to the slope of the observed phase speeds. In other words, with respect to a frame of reference moving at the mean velocity, the velocities of both the rightward- and leftward-propagating waves remain approximately constant. By adding $\bar{U}$ to the predicted phase speed for the Holmboe instability (2.1) we predict the phase speed over the whole channel. This phase speed is shown for both the rightward- and leftward-propagating waves, $c_r^*(x) = \bar{U}(x) \pm 0.83\,\mathrm{cm\,s^{-1}}$, in figure 8(*c*) and matches closely the observed phase speed evolution.

This prediction of the phase speed (figure 8*c*) does not take into account possible changes in J along the length of the channel. However, over the central region of the channel, the variation in J is too small (figure 6*d*) to have a noticeable effect on the wavenumber of maximum growth and the corresponding phase speed.

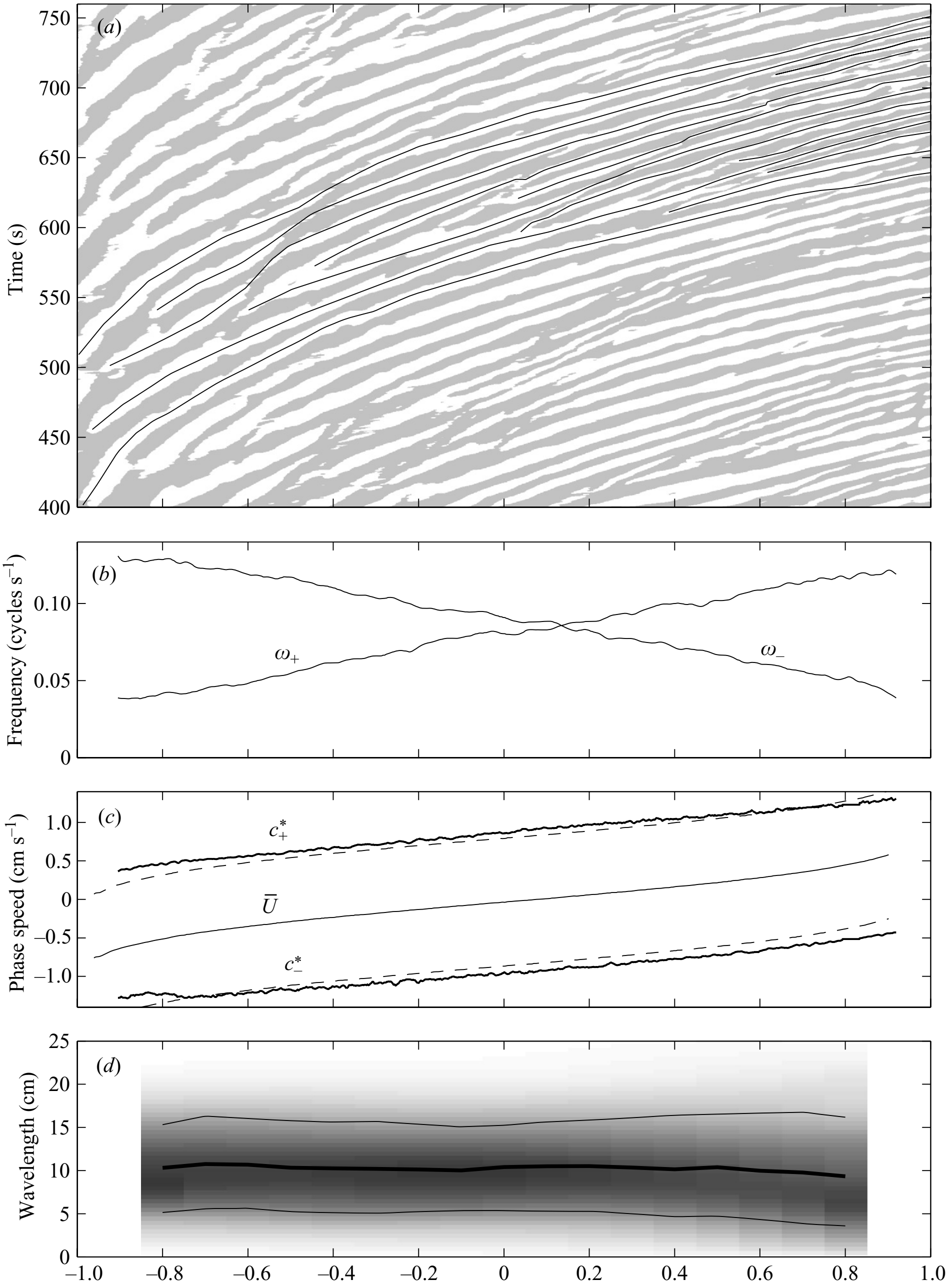

FIGURE 8. (*a*) Characteristics of rightward-propagating waves; grey shading indicates a wave trough, and white indicates a crest. The lines were traced by hand, following individual wave crests. (*b*) The average frequencies of the rightward- and leftward-propagating waves (ω_+ and ω_- respectively) based on zero crossings. (*c*) The thick solid lines represent the phase velocities of the observed rightward-propagating (positive) waves (c_+^*) and leftward-propagating (negative) waves (c_-^*). The thin line shows $\bar{U}$ calculated using the velocity profile and interface height shown in figure 5. The dashed lines are the predicted phase speed of Holmboe instabilities. (*d*) The distribution of the wavelength for the rightward-propagating waves with the average plotted as a heavy line and the 10 and 90 percentiles as thin lines.

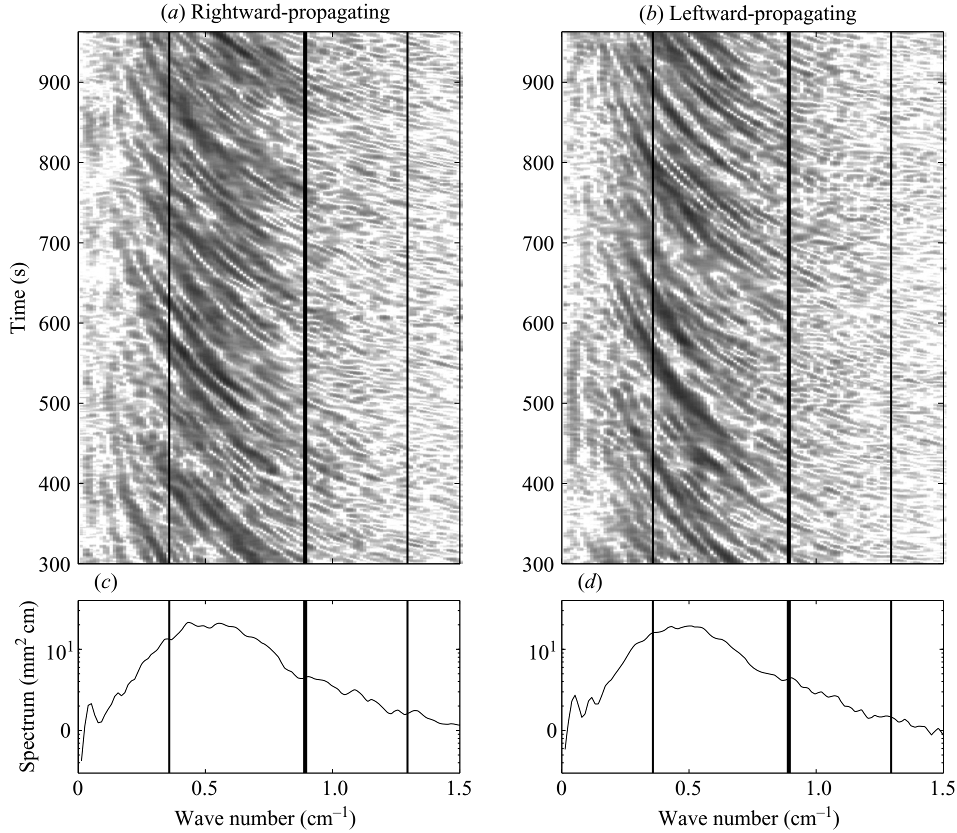

FIGURE 9. Spectra of waves during the steady period between $x = -0.8$ m and $x = 0.8$ m. (a,b) Temporal evolution of the spectra for the rightward- and leftward-propagating waves respectively. The shading is scaled logarithmically from white (low energy) to black (high energy). (c,d) Time-averaged spectrum. The heavy vertical line indicates the wavenumber of maximum growth ($k \approx 0.9\,\mathrm{cm}^{-1}$, $\lambda \approx 7\,\mathrm{cm}$), and the thin vertical lines indicate the stability boundaries ($k \approx 0.36\,\mathrm{cm}^{-1}$, $\lambda \approx 17\,\mathrm{cm}$ and $k \approx 1.3\,\mathrm{cm}^{-1}$, $\lambda \approx 5\,\mathrm{cm}$).

The distribution of wavelength with respect to position is shown in figure 8(*d*) for rightward-propagating waves. The average wavelength and position of all the waves was determined using zero crossings (similar to the frequency in figure 8*b*). The wavelength remains nearly constant ($\lambda \approx 10\,\mathrm{cm}$) throughout x. This is because the two processes, wave formation and wave acceleration, tend to cancel each other out.

Acting by itself, the increase in frequency associated with wave formation will shorten the average wavelength, $\lambda_B = (\omega_A/\omega_B)\lambda_A$, where the subscripts A and B represent different locations in x. The effect of the convective acceleration ($\partial\bar{U}/\partial x$) on the wavelength is not so obvious. As is commonly observed in surface waves (e.g. Peregrine 1976), the acceleration will stretch the waves, increasing their wavelength, i.e. $\lambda_A = (c_A/c_B)\lambda_B$.

Wave stretching is most apparent in the temporal evolution of the wavenumber spectrum (figures 9*a* and 9*b*). Similar to the characteristics, the spectral evolution was determined by compiling the spectrum of the interface height at each time and then contouring. Note that the horizontal axis in figure 9 is the wavenumber, not the

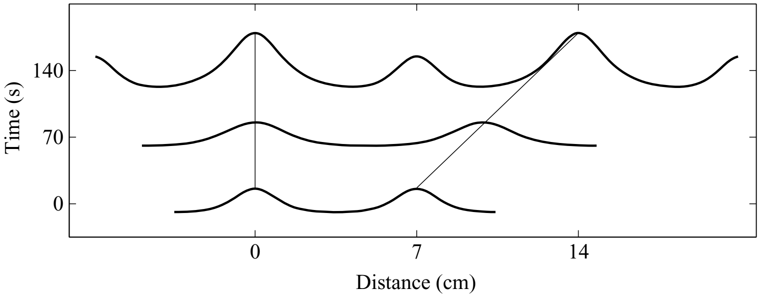

FIGURE 10. Schematic of stretching and formation of rightward-propagating waves. The interface elevation is shown at three times tracking the same wave. The horizontal distance at each time is relative to the trailing crest of the wave. The wave is shown initially with a wavelength equal to the wavelength of maximum growth. Eventually the wave is stretched to twice this length. At the same time new waves form, also at the wavelength of maximum growth. The resulting interface has waves of mixed amplitude and wavelength. The time scale shown for doubling of the wavelength (approximately 140 s) is based on the observations (see figures 9*a* and 9*b*).

distance. The dark (high-energy) diagonal streaks represent energy associated with waves moving through the channel in time (the vertical axis). The slope of the streaks is a result of stretching of individual waves; i.e. waves are continuously decreasing in the wavenumber (increasing in the wavelength).

The time-averaged spectra (figures 9*c* and 9*d*) show the peaks in the wave energy occurring at approximately $0.5\,\mathrm{cm}^{-1}$ ($\lambda = 12.5\,\mathrm{cm}$). The temporal evolution and average spectrum together show the waves form near the wavenumber of maximum growth ($k \approx 0.9\,\mathrm{cm}^{-1}$, $\lambda \approx 7\,\mathrm{cm}$) get stretched and start to lose energy near the lower stability boundary ($k \approx 0.36\,\mathrm{cm}^{-1}$, $\lambda \approx 17\,\mathrm{cm}$).

The two processes, wave stretching and wave formation, are illustrated in the simplified schematic shown in figure 10. The schematic shows the interface elevation at three times. The reference frame ($x = 0$ in the figure) is moving at the speed of the trailing wave crest. As shown in figure 8(*c*) the waves undergo the same convective acceleration as $\bar{U}(x)$. In the central region of the channel this acceleration is approximately $0.005\,\mathrm{s}^{-1}$ (see $\partial\bar{U}/\partial x$ in figure 6*c*). As the pair of crests propagate through the channel the horizontal variation in $\bar{U}$ gives the leading crest a slightly greater phase speed than the trailing crest ($\lambda\ \partial\bar{U}/\partial x = 0.035\,\mathrm{cm\,s}^{-1}$). This difference in phase speed allows the leading crest to pull away from the trailing crest. As the spacing between the two crests (λ) increases, their growth rate decreases (i.e. they are no longer at the wavelength of maximum growth). On the other hand, as the spacing increases the interface between the crests becomes unstable to shorter waves (i.e. waves that are closer to the wavenumber of maximum growth), and a new wave forms. The new waves grow and stretch, and eventually the process repeats itself (see figure 8*a*).

6. Summary and conclusions

Instabilities were investigated using an exchange flow through a long rectangular channel with a rectangular cross-section. The channel connected two large freshwater and saltwater reservoirs. A long period of steady maximal exchange occurred after the cessation of Helmholtz resonance and ended when one of the controls was flooded. During this time symmetric Holmboe instabilities were observed. These instabilities evolved into cusps with a leading elliptical vortex. The vortices drew mixed fluid from the cusp into the free stream. The observed density interface was sharper than, and centred within, the shear layer.

The gradual slope of the interface along the length of the channel resulted in the convective acceleration of each layer. The Holmboe instabilities also accelerated as they propagated through the channel. This acceleration caused the distance between successive cusps to increase, and new waves formed. The new waves formed uniformly along the channel such that the average wavelength remained nearly constant.

By focusing on the central section of the channel we selected the region in which the bulk Richardson number is relatively constant. This, together with the prolonged period of steady exchange and simple channel geometry, resulted in instabilities that had average wave properties that were in good agreement with the linear predictions of Holmboe.

Financial assistance from the Natural Sciences and Engineering Research Council of Canada is gratefully acknowledged. G. A. Lawrence is also grateful for the support of a Canada Research Chair.

REFERENCES

Alexakis, A. 2005 On Holmboe's instability for smooth shear and density profiles. *Phys. Fluids* **17**, 084103.

Armi, L. 1986 The hydraulics of two flowing layers with different densities. *J. Fluid Mech.* **163**, 27–58.

Carpenter, J. R., Lawrence, G. A. & Smyth, W. D. 2007 Evolution and mixing of asymmetric Holmboe instabilities. *J. Fluid Mech.* **582**, 103–132.

Farmer, D. M. & Armi, L. 1998 The flow of Atlantic water through the Strait of Gibraltar. *Prog. Oceanogr.* **21**, 1–98.

Geyer, W. R. & Smith, J. D. 1987 Shear instability in a highly stratified estuary. *J. Phys. Oceanogr.* **17**, 1668–1679.

Gu, L. & Lawrence, G. 2005 Analytical solution for maximal frictional two-layer exchange flow. *J. Fluid Mech.* **543**, 1–17.

Hogg, A. McC. & Ivey, G. N. 2003 The Kelvin–Helmholtz to Holmboe instability transition in stratified exchange flows. *J. Fluid Mech.* **477**, 339–362.

Holmboe, J. 1962 On the behaviour of symmetric waves in stratified shear layers. *Geofys. Publ.* **24**, 67–112.

Koop, C. G. & Browand, F. K. 1979 Instability and turbulence in a stratified fluid with shear. *J. Fluid Mech.* **93**, 135–159.

Lawrence, G. A., Browand, F. K. & Redekopp, L. G. 1991 The stability of a sheared density interface. *Phys. Fluids* **3** (10), 2360–2370.

Miles, J. & Munk, W. 1961 Harbor paradox. *J. Waterways Harb. Am. Soc. Civ. Engrs WW3* **87**, 111–130.

Peregrine, D. H. 1976 Interaction of water waves and currents. *Adv. Appl. Mech.* **16**, 9–117.

Pouliquen, O., Chomaz, J. M. & Huerre, P. 1994 Propagating Holmboe waves at the interface between two immiscible fluids. *J. Fluid Mech.* **266**, 277–302.

Smyth, W. D. 2006 Secondary circulations in Holmboe waves. *Phys. Fluids* **18** (064104), 1–13.

Smyth, W. D., Carpenter, J. R. & Lawrence, G. A. 2007 Mixing in symmetric Holmboe waves. *J. Phys. Oceanogr.* **37**, 1566–1583.

Smyth, W. D. & Winters, K. B. 2003 Turbulence and mixing in Holmboe waves. *J. Phys. Oceanogr.* **33**, 694–711.

Tedford, E. W., Carpenter, J. R., Pawlowicz, R., Pieters, R. & Lawrence, G. A. 2009 Observation and analysis of shear instability in the Fraser River Estuary. *J. Geophys. Res.* Accepted subject to revision.

Thorpe, S. 1971 Experiments on instability of stratified shear flows: miscible fluids. *J. Fluid Mech.* **46**, 299–319.

Wesson, J. C. & Gregg, M. C. 1994 Mixing at Camarinal Sill in the Strait of Gibraltar. *J. Geophys. Res.* **99**, 9847–9878.

Yoshida, S., Ohtani, M., Nishida, S. & Linden, P. F. 1998 Mixing processes in a highly stratified river. In *Physical Processes in Lakes and Oceans*, *Coastal and Estuarine Studies* (ed. J. Imberger), vol. 54, pp. 389–400. American Geophysical Union.

Zhu, D. & Lawrence, G. A. 2001 Holmboe's instability in exchange flows. *J. Fluid Mech.* **429**, 391–409.